The University of Glasgow

Masters Thesis

Silicon Photonic Waveguides & Nonlinear Optical Effects

Author:
Sean Tabor

Supervisor:
Prof. Marc Sorel

University of Glasgow

A thesis submitted in fulfilment of the requirements for the degree of Master of Research

in the

School of Engineering

June 2018

THE UNIVERSITY OF GLASGOW

Abstract

Electronics and Electrical Engineering
School of Engineering

Master of Research

Silicon Photonic Waveguides & Nonlinear Optical Effects

by Sean Tabor

Second-order nonlinear effects in silicon have shown great promise for producing all-optical, silicon, CMOS compatible modulators and optical interconnects. This project aims to investigate the enhancement of $\chi^{(2)}$ in silicon due to different waveguide geometries and cladding layers. Initial work will focus on quantifying second-harmonic generation in strip and slot waveguides, and analysing how the different waveguide geometries can enhance this effect.

Acknowledgements

I would greatly like to thank Professor Marc Sorel for his wealth of knowledge, support, and advice during my time as a PhD student, as well as providing me with this great opportunity. I would also like to thank Dr Graham Sharp for his steadfast friendship and encouragement throughout my time at Glasgow university. Finally, I would like to express my immense gratitude towards my family for their unwavering love and support.

Contents

List of Figures

List of Tables

Abbreviations

BEOL	**B**ack **E**nd **O**f **L**ine
CMOS	**C**omplimentary **M**etal **O**xide **S**emiconductor
ER	**E**xtinction **R**atio
FCA	**F**ree **C**arrier **A**bsorption
FCPD	**F**ree **C**arrier **P**lasma **D**ispersion
FWM	**F**our **W**ave **M**ixing
GVD	**G**roup **V**elocity **D**ispersion
GVM	**G**roup **V**elocity **M**ismatch
IC	**I**ntegrated **C**ircuit
OPO	**O**ptical **P**arametric **O**scillator
SHG	**S**econd **H**armonic **G**eneration
SOH	**S**ilicon **O**rganic **H**ybrid
SOI	**S**ilicon **O**n **I**nsulator
SPDC	**S**pontaneous **P**arametric **D**own **C**onversion
SPM	**S**elf **P**hase **M**odulation
SRS	**S**timulated **R**aman **S**cattering

SWG	**S**ub **W**avelength **G**rating
TE	**T**ransverse **E**lectric
THG	**T**hird **H**armonic **G**eneration
TIR	**T**otal **I**nternal **R**eflection
TM	**T**ransverse **M**agnetic
TPA	**T**wo **P**hoton **A**bsorption
XPM	**C**ross **P**hase **M**odulation

Symbols

ω	angular frequency	$rads^{-1}$
n	refractive index	
Δ^2_{xy}	Laplace operator	
c	speed of light	ms^{-2}
β	propagation constant	
α	attenuation constant	dB/cm
$\vec{P}$	induced dipole polarisation moment	$C.m$
$\vec{E}$	electric field	V/m
ε_o	permittivity of free space $= 8.85 \times 10^{-12}$	F/m
$\chi^{(2)}$	second-order dielectric susceptibility	m/V
λ	wavelength	m
$\eta_{2\omega}$	SHG efficiency	
k	wavenumber	m^{-1}
Δk	phase mismatch	m^{-1}

Introduction

1.1 Overview of Research

1.1.1 Silicon as an Optical Material

Silicon photonics is set to revolutionise the microelectronics industry in at least some areas; most large micro-electronic industries are already establishing programs for silicon photonics using existing tools[1]. As a semiconductor material, silicon has been used extensively for electronic applications. However, silicon possesses multiple properties which are advantageous for use as an optical material:

- Transparent window suitable for optical communication (between 1.2 - 6.5 μm)
- High refractive index (allows for compact structures)
- Low cost
- Extensively studied material and mature technology
- CMOS compatible

Here CMOS stands for complementary metal-oxide-semiconductor, and it is the process by which integrated circuits (ICs) are produced. Additionally, silicon is the backbone of the IC industry and, therefore, makes it a highly suitable material for achieving integration between photonics and microelectronics. Nevertheless, silicon also has its limitations, these include:

- Lack of detection (absorption) around 1.5 μm
- High index contrast can cause difficulties for efficient optical coupling
- Very small electro-optic effect
- Very low quantum efficiency (poor light emission)

These limitations, however, have not hindered the research into silicon photonics, and as a relatively new field, there is the potential for it to greatly improve technology in domestic and industry/research environments.

1.1.2 Second-harmonic Generation and Slot Waveguides

Second-harmonic generation (SHG) is an ultra-fast process which can be used for sum-frequency generation and difference frequency generation (explained further in Sec. 2.1). Another ultra-fast nonlinear effect that is commonly used for optical modulation is the Kerr effect[2]. SHG has advantages over the Kerr effect in that it operates at a much lower power, exhibits a linear electro-optic effect (which is important for analogue modulation), and can utilise less complex pumping schemes; for example, SHG can be produced with only one pump).

SHG has already been shown to produce optical modulators in silicon[3]. Some research groups have also been using slot waveguides to create silicon-organic-hybrid (SOH) which exploit the electric field profile of slot waveguides to excite a deposited, highly nonlinear, material to achieve fast modulation speeds[4]. The slot waveguide is therefore of particular interest and will be discussed in Sec. 4.

1.2 Brief History

1.2.1 Success of Microelectronics

Before discussing silicon photonics in detail, it is important to understand why microelectronics has been so successful and why the addition of photonics may be needed to continue this success. It could be said that microelectronics was born with the creation of the first (germanium) transistor in 1947. However, it wasn't until 1961 that the emergence of the first planar integrated circuit (IC) was seen[5]. The following production of ICs resulted in the, now famous, Moore's laws that states the number of transistors per chip will double every 19 months[6]. Impressively, the microelectronics industry has kept pace with Moore's law, to the point where computer processors now contain billions of transistors[7]. However, the complexity of this technology has introduced limitations to these devices, limitations which may only be overcome by employing photonic based solutions.

By holding to Moore's law, computer processors have developed into intricate, multi-core and multi-layered devices. This increase in complexity can be seen by looking at the increase in the number of layers present in a typical chip over time.

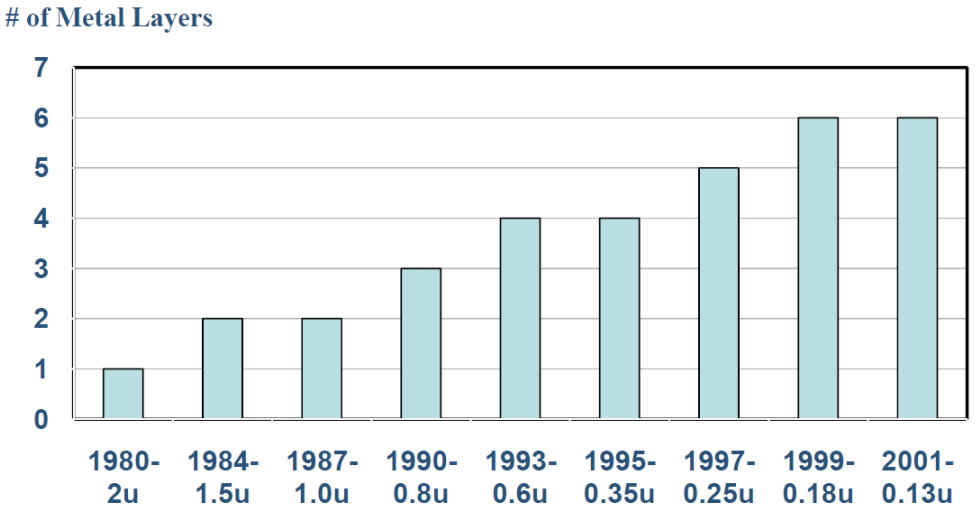

FIGURE 1.1: Graph showing the trend of increasing metal layers over time, with the semiconductor manufacturing process used for each year noted below[8]

As the number of metal layers within the chip increase, the total length of the metal interconnects within the chip also increases. Metal interconnects are (mostly) produced in the back end of line (BEOL) portion of chip fabrication. This is where individual devices (i.e. transistors, resistors, etc.) are interconnected and wired to the wafer to make a complete device. These wires are what are referred to as interconnects. Due to its easier patterning during fabrication,

aluminium was originally used as the metal for these interconnects. However, following advances in fabrication techniques, copper has become the industry standard due to its higher conductivity compared to aluminium[9].

1.2.2 The Interconnect Problem

As seen in Fig. 1.2a, the current total interconnect lengths are reaching the 10 km mark[10], at which length, significant challenges start to arise. This includes problems such as power dissipation and propagation delay[11] (interconnect bottleneck), the former impacting efficiency and the later impacting performance. Fig. 1.3a shows the increasing power requirements for evolving generations of processors. One way to decrease the power consumption is by lowering the CPU operating voltage.

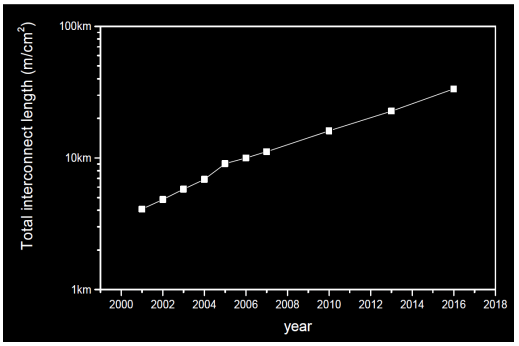

(A) Graph indicating the trend of increasing metal interconnect length with time[8] (source data derived from ITRS interconnect tables[12])

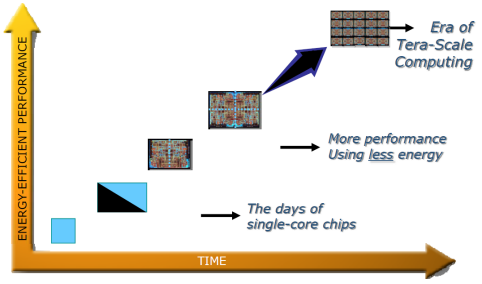

(B) Prediction of massively parallel multi-core processors due to trend of increasing processor cores to achieve better power efficiency

FIGURE 1.2

However, as can be seen in Fig. 1.3b, the voltage scaling which allows for this is also diminishing which highlights power dissipation/requirements as a major problem for the future when using metal interconnects. One way of minimising power dissipation was to create processors with parallel multi-core architectures.

Instead of a single complex processor, these are comprised of multiple, simpler, processing cores. This results in a much improved performance per Watt. However, power losses due to the metal interconnects are still high in these devices; many chips lose approximately 30-50% of power due to interconnects[13].

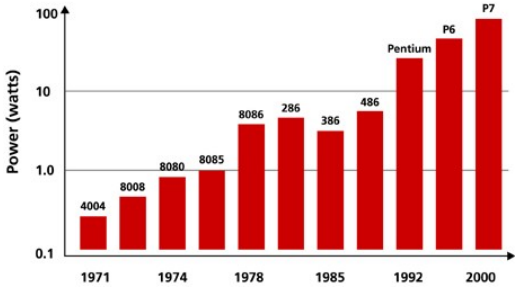

(A) Graph showing increasing power requirements for evolving generations of processor[14]

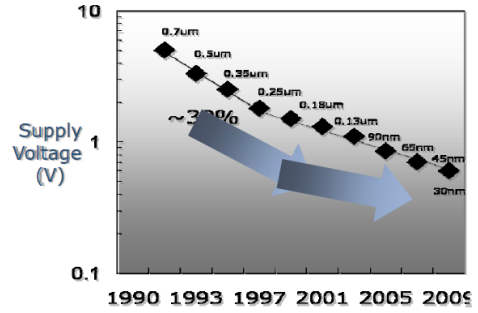

(B) Graph showing the trend of decreased voltage scaling with progressing generations of processor[8]

FIGURE 1.3

If the trend of adding more cores to achieve increased energy efficient performance continues, as depicted in Fig. 1.2b, it is possible that this will result in massively parallel future devices. As the level of parallelisation increases, so does the interconnect length. Therefore, optical interconnects may become a necessity for two reasons: to maintain high speed intra-chip communication and to avoid high levels of power dissipation. Nevertheless, merging photonics with microelectronics does not come without challenges, which include:

- How to merge photonics and electronics?
- How to move optical communications to the chip?
- How to standardise photonics?

An answer to these challenges may lie with silicon photonics. To help elucidate why silicon photonics in particular is the best candidate for integration with microelectronics, it is beneficial to examine photonics as a whole, to understand why it has not achieved the same industrial success as microelectronics.

1.2.3 Growth of Photonics

Following a fibre optic breakthrough in 1966, photonics was later designated as a separate technology in 1970. Further breakthroughs in fibre optics, as well as semiconductor lasers, led to the emergence of optical communications (i.e. telephone and eventually internet). The evolution of photonics over the past few decades is shown in Fig. 1.4, which also contains information for microelectronics (for comparison) and nonlinear silicon photonics which will be discussed later.

As can be seen in Fig. 1.4, the arrival of photonics was close to that of microelectronics and the IC. The reason photonics did not achieve mass manufacturing on a similar scale to that of its electrical counterpart was due to a lack of integration caused by the diverse nature of the field. Tab. 1.1 displays a comparison of the two fields in terms of building blocks, material base, and manufacturing processes. From this table, it can be seen that photonics has a much greater variety compared to the strict ingredients for making ICs. Consequently, photonics has evolved to generate highly specialised devices for particular applications, which are packaged separately and connected via fibre afterwards if needed. These components utilise numerous types of material as well, for example: glass for optical multiplexers, lithium niobate for modulators, indium phosphide for lasers, and germanium for photodetectors. As a result of using different materials, many photonic components have incompatible manufacturing processes, with speciality fabrication facilities used for certain devices[15]. The overall effect of this is extremely difficult integration with ICs, high costs for photonic components and systems, and low-volume production (compared to the electronics industry) for most photonic devices.

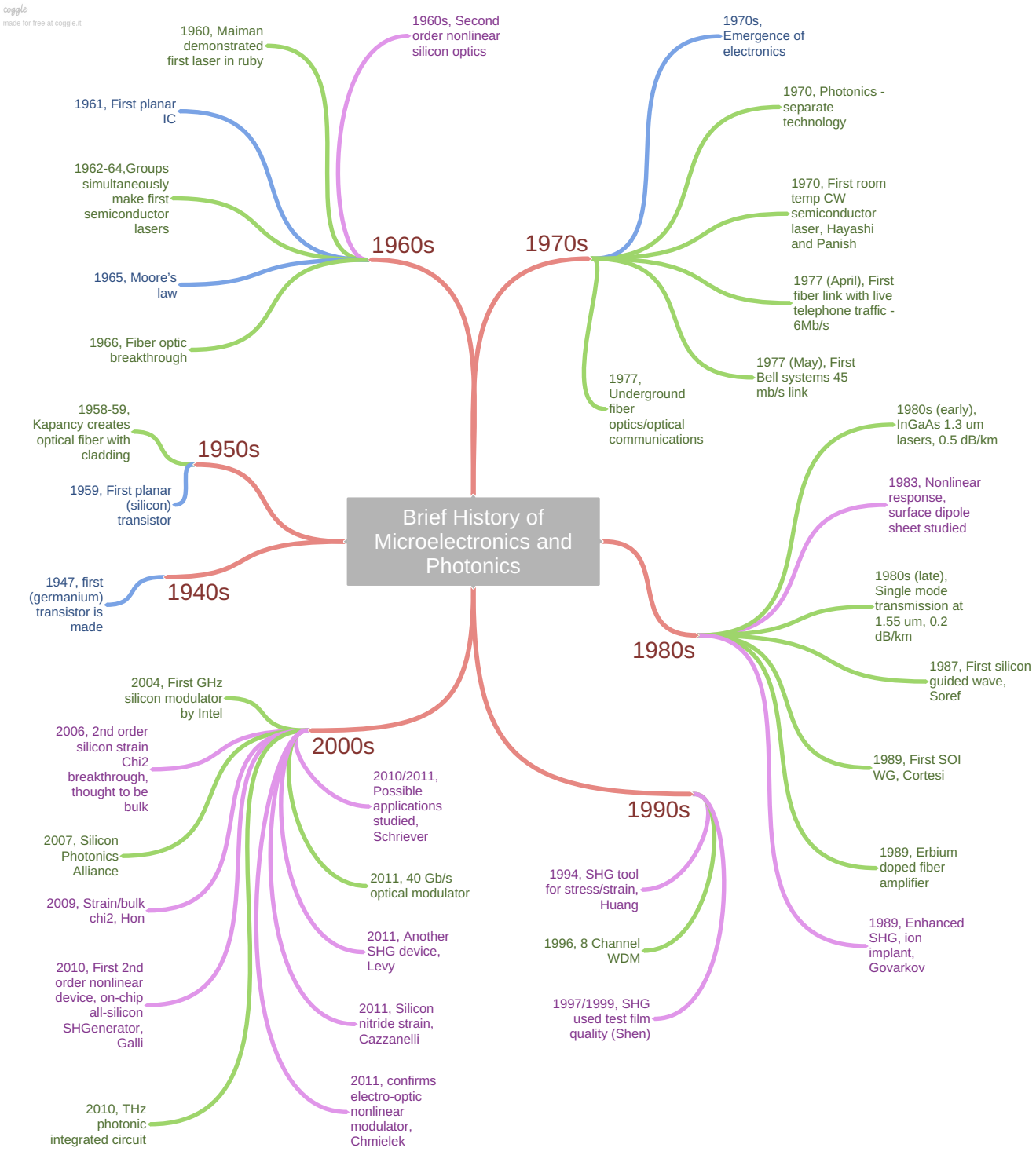

FIGURE 1.4: Branched timeline showing the evolution of microelectronics (blue), photonics (green), and nonlinear effects in silicon (purple)

Comparison of Various Technologies

	Microelectronics	Photonics	Silicon Photonics
Building blocks	Transistor	Laser, photodetector, modulator, optical fiber, waveguide, DWDM, etc.	Laser, waveguides, modulator, microresonators
Material	Silicon[a]	Semiconductors, glasses, polymers, insulators, etc.	Silicon[a]
Manufacturing technology	CMOS	Epitaxy, deposition, glass drawing, ionic diffusion, etc.	CMOS compatible process[b]

TABLE 1.1: Comparison of the different types, and number, of components that comprise microelectronics, photonics, and silicon photonics[1]

As mentioned previously, the increasing length of metal interconnects posses a significant problem for the future of microelectronics. Coupling this with consumer desires for faster internet and computers (i.e. increased bandwidth), provides a clear driving force for the integration of photonics. There are some very good reasons why silicon photonics may be the best candidate for achieving this. Firstly, silicon is an optical material, and can therefore be used to create active or passive optical devices. Secondly, and arguably the most important, is that it is also compatible with CMOS processing. This allows existing, expensive, IC tools and processes to be used instead of inventing new/specialist ones.

Consequently, this could lead to a standardisation for the production of integrated monolithic photonic based devices, with the potential to yield similar success to that of microelectronics (high volume production at low cost) due to the CMOS compatibility of silicon.

As mentioned previously, the vast majority of current photonics devices do not lend themselves easily to large scale production. Contrastingly, a large amount of the success of microelectronics stemmed from its standardisation, which allowed small companies or research groups to submit their ideas for fabrication (be it an industrial partner or other fabrication centre) and quickly move them to large scale production if successful[15]. By restricting photonics to a single material (silicon) and a set manufacturing process (CMOS), as seen in Tab. 1.1, the chances of successfully copying the microelectronics model are greatly increased. This could be achieved by standardising the production of integrated monolithic photonic based devices, resulting in high volume production for photonic components and systems.

A replacement for metal interconnects would come in the form of silicon optical interconnects (see Sec. 1.3.1). For integration into current systems, and for future all-optical monolithic devices, there will be the need for optical components which can generate, detect, modulate, and manipulate light. These components already exists using non-silicon materials, and much of the research into silicon photonics is aimed at developing silicon based alternatives with equal or greater performance[16].

1.3 Photonic Components

For silicon photonics to be successful, it will need to generate optical components which either match or better their electronics counterparts. This will require components with low power dissipation, small latency, and of suitably compact size. The type of optical components that are needed include: interconnects, modulators, couplers, splitters/combiners, detectors, and lasers.

1.3.1 Optical Interconnects: Waveguides

Waveguides are one of the most important optical components as they would function as the replacement for metal interconnects. Amongst other pioneering work carried out on silicon in the 1980s by Soref *et al.*, was the first guided light wave in silicon[17]. This is achieved by confining the light via total internal reflection (TIR); light is injected into a core which is surrounded by a lower refractive index cladding, shown in Fig. 1.5a.

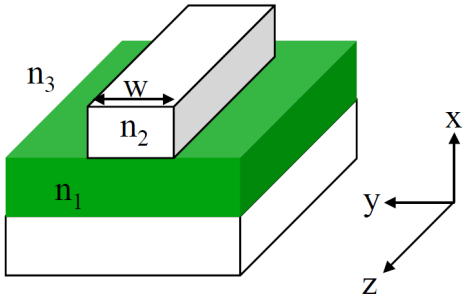

(A) Example of a SOI strip waveguide (green = SiO_2, white = Si), where $n_2 > n_1 > n_3$

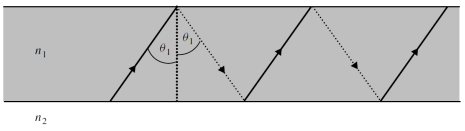

(B) Diagram showing waveguide propagation due to total internal reflection[18]

FIGURE 1.5

The propagation of light through the waveguides which have dimensions $W << \lambda$, can be derived via the Helmholtz equation (Eqn. 1.3.1).

$$(\boldsymbol{\Delta}_{xy}^2 + \beta_m^2)\mathbf{e}_m(x,y,z) = \frac{\omega^2}{c^2} n^2(x,y)\mathbf{e}_m(x,y,z) \tag{1.3.1}$$

In this equation, $\Delta_{x,y}$ is the Laplace operator in the x and y dimensions, β_m is the modal propagation constant given by Eqn. 1.3.2, $\mathbf{e}_m(x,y,z)$ is the electric field present inside the waveguide, and $n(x,y)$ is the refractive index profile inside the waveguide.

$$\beta_m = \frac{\omega}{c} n_{eff,m} \tag{1.3.2}$$

The propagation constant contains the effective refractive index, n_{eff}, which is necessary for waveguides as dispersion is not only determined by material properties but also by the geometrical properties of the waveguide. The subscript m denotes the order of mode travelling through the waveguide; these modes result from discrete solutions of the Helmholtz equation. Different modes will also result in a different effective refractive index due to the different amount of modal confinement. Modes are classed as either TE or TM. In general, for sub-wavelength waveguides, the type of mode is determined by the polarisation of the electric field being input into the waveguide[18], where the convention is usually, with reference to Fig. 1.5a, TE in the y-direction and TM in the x-direction. Any attenuation through the waveguide is given by the attenuation constant (α), shown in Eqn. 1.3.3.

$$\alpha = \frac{2\omega}{c} Im[n_{eff,m}] \tag{1.3.3}$$

The dispersion ($n_{eff,m} \propto \lambda$) of a particular waveguide depends on numerous factors:

- mode order
- waveguide geometry
- polarisation
- core/cladding material (chromatic dispersion)

These factors can be adjusted in a process called dispersion engineering in order to achieve the desired result from the waveguide (i.e. single mode operation at 1.55 μm).

1.3.2 Optical Modulators

In simple terms, an optical modulator is a device which can encode information onto an optical signal via an external command (i.e. an electric signal). The performance metrics for optical modulators can be split into the following factors:

- extinction ratio
- insertion loss
- power consumption
- optical bandwidth
- footprint

Here, the extinction ratio (ER) is a measure of the maximum to minimum signal intensity, with a high ER being beneficial for transmission over long distances and low bit error rates. Insertion loss is a measure of the loss introduced to the system due to the addition of the device. Power consumption is measured in fJ/bit and is an important consideration due to the interconnect problem discussed previously. The optical bandwidth indicates the useful wavelength range of the device and the footprint is the physical space that the device occupies.

There are typically two main types of modulation used in silicon optical modulators: electro-absorption and electro-refraction. The former modulates the light signal via changes in amplitude by inducing a change in absorption of the material in which the light propagates. The latter influences the phase of the light to achieve modulation. These forms of modulation are most commonly exploited by using one of the following effects: thermo-optic, free-carrier plasma dispersion (FCPD), SHG, Kerr effect, Franz-Keldysh effect, or the quantum-confined Stark effect. This report will focus mainly on the SHG (discussed in detail in Sec. 2), however, further information about the mentioned effects and their applications in silicon modulators can be found in the review paper by Reed *et al.*[18]

Fundamentals of Nonlinear Optics

Nonlinear optics is used to describe the behaviour of light when the induced dipole polarisation moment ($\vec{P}$) of a material responds nonlinearly to the presence of an electric field ($\vec{E}$), either from the light itself or from an externally applied field[2].

2.1 Second-harmonic Generation and Kerr Effects

A brief derivation of the second-harmonic generation (SHG) can be started from the expression for the induced dipole polarisation moment shown in Eqn. 2.1.1:

$$\vec{P} = \varepsilon_o \chi \vec{E} \tag{2.1.1}$$

Eqn. 2.1.1 is used for normal, linear, circumstances, where χ is the dimensionless dielectric susceptibility and the electric field can be assumed to have the form shown in Eqn. 2.1.2:

$$E(t) = E_\omega cos(\omega t) \tag{2.1.2}$$

In this equation E_ω denotes the maximum amplitude of the electric field in the light wave. However, as light intensity increases, the linear model for induced dipole polarisation constant is no longer accurate. Therefore, taking a power series of Eqn. 2.1.1 yields a new equation for $\vec{P}$, Eqn. 2.1.3:

$$\vec{P} = \varepsilon_o(\chi^{(1)}\vec{E} + \chi^{(2)}\vec{E^2} + \chi^{(3)}\vec{E^3} + ..) \tag{2.1.3}$$

Here, $\chi^{(n)}$ is a tensor of rank n which defines the dielectric susceptibility; $\chi^{(2)}$ and $\chi^{(3)}$ correspond to nonlinear effects. Focussing only on first and second order terms and substituting in Eqn. 2.1.2 while simultaneously using the trigonometric identity $cos^2\theta = 1/2(1 + cos(2\theta))$ yields Eqn. 2.1.4:

$$\vec{P} = \varepsilon_o \chi^{(1)} E_\omega cos(\omega t) + \chi^{(2)} E_\omega^2 (1/2 + 1/2 cos(2\omega t)) \tag{2.1.4}$$

The induced dipole moment shown in Eqn. 2.1.4 now consists of three terms which can be first order and second order (nonlinear) effects:

- $\varepsilon_o \chi^{(1)} E_\omega cos(\omega t) \Rightarrow P \propto E_\omega$ (linear), oscillating at ω
- $1/2\chi^{(2)} E_\omega^2 \Rightarrow P \propto E_\omega^2$ (nonlinear), non-oscillating term
- $1/2\chi^{(2)} E_\omega^2 cos(2\omega t) \Rightarrow P \propto E_\omega^2$ (nonlinear), oscillating at 2ω

Therefore, Second-harmonic generation (SHG) is shown here by the term oscillating at 2ω (within the two nonlinear expressions), where $\chi^{(2)}$ is the second order susceptibility which defines the magnitude of the SHG. Other phenomena can also be observed if the input electric field contains more than one optical frequency i.e. $E = E_1 + E_2$, oscillating at frequencies ω_1 and ω_2 respectively. In this situation, and solving the above equations in the same manner, would then result in $\vec{P}$ consisting of five frequencies: 0, $2\omega_1$, $2\omega_2$, $\omega_1 + \omega_2$, $\omega_1 - \omega_2$, where $\omega_1 + \omega_2$ and $\omega_1 - \omega_2$ are know as frequency down-conversion and frequency up-conversion (or sum-frequency generation) respectively.

By considering the third order terms in Eqn. 2.1.3, the same method can be used to solve for the third order $\chi^{(3)}$ terms which correspond to the Kerr effect. The result of which is a wide variety of phenomena:

- Self-phase modulation (SPM)
- Cross-phase modulation (XPM)
- Third-harmonic generation (THG)
- Four-wave mixing (FWM)
- Stimulated Raman scattering (SRS)
- Two-photon absorption (TPA)

A great explanation of these phenomena can be found in the review paper by Leuthold[19] *et al.* on nonlinear silicon photonics. The textbook "Nonlinear Optics" written by Robert W. Boyd also provides a comprehensive explanation of these topics[20]. One important point to note however, is that TPA and the associated free-carrier absorption (FCA), increase the amount of absorption and limit the speed of silicon photonic devices[21]. Notably, these processes are much weaker for the Pockels effect compared to the Kerr effect[19].

2.2 Second-harmonic Generation in Silicon and Centrosymmetry

Second-harmonic generation (SHG) is usually not exhibited in crystal structures with centrosymmetry. The reason can be explained in terms of the light interacting with itself inside the crystal structure; light that has entered the crystal structure (at ω) will, unlike the linear regime, interact with oscillations of the crystal structure that have been caused by the light that preceded it. As is the nature of SHG, these oscillations can occur at 2ω, therefore, the sum

of these two frequencies is illustrated in Fig. 2.1. As can be seen from this figure, the result is an asymmetric response; since centrosymmetric means the structure exhibits inversion symmetry, it is therefore not possible (in the electric-dipolar approximation) for a centrosymmetric structure to oscillate in the same asymmetric manner.

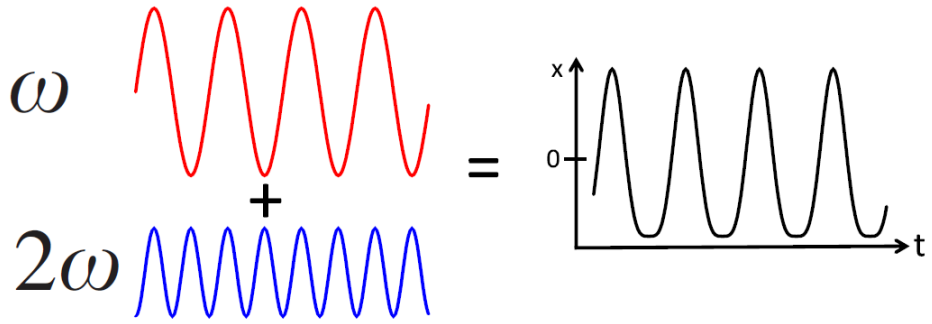

FIGURE 2.1: Sum of fundamental and second harmonic frequencies during SHG, results in an anharmonic oscillation[22]

It has been shown however, that there is a bulk second-order susceptibility in silicon due to a quadrupolar interaction, an explanation of which can be found in this review paper by Cazzanelli[22]. Silicon also produces a surface $\chi^{(2)}$ due to the abrupt end of the crystal structure (first few hundreds of nanometres[1]) and resulting break of symmetry. These two contributions are the source of second-order SHG which has been observed since the 1960s. Breaking the crystal symmetry acts to increase the magnitude of SHG, and has therefore been the focus of much recent research which will be elaborated on in Sec. 3

2.3 SHG Intensity

The relation for SHG efficiency ($\eta_{2\omega}$) is shown in Eqn. 2.3.1[2], where the maximum efficiency ($\eta_{2\omega}^{max}$) is given by Eqn. 2.3.2.

$$\eta_{2\omega} = \eta_{2\omega}^{max} sinc^2(\Delta kL/2) \tag{2.3.1}$$

$$\eta_{2\omega}^{max} = \frac{8\pi^2 d_{eff}^2 L^2 I_\omega}{\varepsilon_o n_\omega^2 n_{2\omega} c \lambda_\omega^2} \tag{2.3.2}$$

In Eqns. 2.3.1 and 2.3.2, Δk is the phase mismatch, L is the length of the waveguide, d_{eff} is the second-order susceptibility, I_ω is the intensity of the fundamental mode, n_ω and $n_{2\omega}$ are the refractive indices of the fundamental and second-order modes respectively, and λ_ω is the fundamental wavelength.

For light propagating through a waveguide, the wavenumber, k, should be replaced with the waveguide phase constant, β, and the refractive index, n, should be replaced with the effective refractive index, n_{eff}. For the sake of simplicity, the following relations will be kept consistent with the notation of Eqns. 2.3.1 and 2.3.2. The phase mismatch for SHG is given by Eqn. 2.3.3, where k_ω and $k_{2\omega}$ are the wavenumbers of the fundamental and second-order modes respectively.

$$\Delta k = k_3 - k_1 - k_2 = k_{2\omega} - 2k_\omega \tag{2.3.3}$$

For propagation in the z-direction, efficient SHG will only be produced if the fundamental and second-harmonic waves interfere constructively at any point, say z_o, along the waveguide. Imposing this condition (and using the relations $k = \frac{\omega}{v_p}$ and $v_p = \frac{c}{n}$) leads to the phase-matching condition shown in Eqn. 2.3.4.

$$\begin{aligned} k_{2\omega} z_o &= 2k_\omega z_o \\ \frac{2\pi}{\lambda/2} n_{2\omega} &= 2\frac{2\pi}{\lambda} n_\omega \\ n_{2\omega} &= n_\omega \end{aligned} \tag{2.3.4}$$

Inserting this condition into Eqn. 2.3.3 yields the equation for the phase mismatch in terms of fundamental wavelength and the refractive indices of the two modes, shown in Eqn. 2.3.5 below.

$$\begin{aligned} \Delta k &= k_{2\omega} - 2k_\omega \\ &= \frac{2\pi n_{2\omega}}{\lambda/2} - \frac{2(2\pi n_\omega)}{\lambda} \\ &= \frac{4\pi n_{2\omega}}{\lambda} - \frac{4\pi n_\omega}{\lambda} \\ \Delta k &= \frac{4\pi}{\lambda}[n_{2\omega} - n_\omega] \end{aligned} \tag{2.3.5}$$

Therefore, with knowledge of the dispersive properties, the above equation can be used to calculate the SHG efficiency by inserting the values of Δk into Eqn. 2.3.1. The phase-matching bandwidth can also be considered by Taylor expanding Eqn. 2.3.5 around the point $\lambda = \lambda_o + \delta\lambda$, with phase-matching assumed at λ_o (meaning $n(\lambda_o) = n(\lambda_o/2)$). This yields Eqn. 2.3.6.

$$\Delta k(\lambda) = \frac{4\pi\delta\lambda}{\lambda_o}\left[\frac{\delta n(\lambda_o)}{\delta\lambda} - 1/2\frac{\delta n(\lambda_o/2)}{\delta\lambda}\right] \tag{2.3.6}$$

Therefore, the phase-matching bandwidth ($\delta\lambda_{FWHM}$), defined by full width at half maximum (FWHM) of Eqn. 2.3.1, can be solved for by inserting $|\Delta k_{BW}| = 2.784/L$ (since $sinc^2(1.39) = \frac{1}{2}$) into Eqn. 2.3.6 and rearranging for $\delta\lambda_{FWHM}$, and is given by Eqn. 2.3.7 below.

$$\delta\lambda_{FWHM} = \frac{0.22\lambda_o/L}{|\frac{\delta n(\lambda_o)}{\delta\lambda} - 1/2\frac{\delta n(\lambda_o/2)}{\delta\lambda}|} \tag{2.3.7}$$

Eqn. 2.3.7 can also be derived in terms of the group velocity mismatch or GVM (defined as the difference between the inverse of the group velocities). The GVM can cause broadening or compression of ultrashort pulses (along with the group velocity dispersion (GVD)), and can therefore be responsible for limiting the bandwidth even when phase-matching has been carried out (i.e. when $\Delta k = 0$).

Cutting Edge Research

In order to have a clear picture of the research field, the most up-to-date and significant research regarding second-order nonlinear silicon photonics will be presented in this section, with an evolution of the topic covered beforehand. As well as providing a deeper insight into the topic, this summary of the literature will provide a clear benchmark for enhanced $\chi^{(2)}$ values achieved in silicon devices.

3.1 Second-harmonic Generation in Silicon Photonic Devices

The second-order nonlinear responses from from silicon, and its centrosymmetric structure, have been studied since the 1980s; Shen et al. were the first group to study the surface dipolar repsonse, and bulk quadrupolar response via reflection measurements[23]. These second-order nonlinear responses from unmodified crystalline silicon are very weak ($\chi^{(2)}_{surface} = 10^{-2}\ pm/V$ and $\chi^{(2)}_{bulk} = 10^{-}7\ pm/V$) and is the reason why it is not normally considered a second-order nonlinear material. For example the second-order susceptibilities of $LiNbO$ and $GaAs$ reach up to $\approx 368\ pm/V$ and $\approx 34\ pm/V$ respectively[2]. A few years later, Govorkov et al. were the first to test the effects of deforming the crystal structure on the surface of the silicon through SHG experiments[24]. The deformation, and hence breaking of the crystal symmetry, were achieved by either ion implantation or the application of a stressing layer (i.e. SiO_2) on top of the silicon. Both of these techniques resulted in an enhancement of the SHG, generated by *surface* second-order effects. Following this, it was later shown that the SHG signal could be used to derive information about the stress/strain in the deformed layer[25], which then progressed as use as a tool for testing the surface film quality of silicon[26].

The first reported results of an enhanced *bulk* second-order effect (opposed to the weak bulk quadrupolar $\chi^{(2)}$ in silicon[22]) were published in 2006 by Jacobsen *et al.*[27] ($\chi^{(2)} \approx 15\ pm/V$). The possibility of achieving a significant bulk $\chi^{(2)}$ in silicon had the effect of creating renewed focus on nonlinear effects in silicon. Ways to exploit these nonlinear effects in silicon were studied by Schriever *et al.*[28], and the first all-silicon device to employ nonlinear surface

effects was achieved by Galli *et al.* in 2010[29]. Since then, many research groups have reported different values of surface and bulk $\chi^{(2)}$ values, a comparison of the most significant results has been compiled in Tab. 3.1.

One important paper to mention is that published by Azadeh *et al.* in 2015[30]. This followed a previously published paper that proposed a third-order non-linear effect resembling that of a second-order effect was actually contributing to the $\chi^{(2)}$ value when a silicon nitride stressing layer was used[31]. This was experimentally proven in the paper by Azadeh *at al.*, indicating that free carriers and surface charging had a large part to play in the measured $\chi^{(2)}$ values when a silicon nitride overlayer is used. This had a significant impact on the field as it is likely the $\chi^{(2)}$ results from previous work do not include this contribution. This has been considered in Tab. 3.1, and results that most likely contain an unquantified contribution from surface layer charging during DC measurements (i.e. a direct voltage applied onto the waveguides via electrodes) have been marked in red. The contribution from this charging effect (also know as EFISH, standing for electric field induced second harmonics generation) in all-optical experiments is unclear, and has been shaded yellow in Tab. 3.1. Further evidence of the presence of the EFISH effect was proven by Borghi *et al.* via high speed measurements[32]. Additionally, Timurdogan *et al.*[33] have utilised this effect to produce the most efficient (at $P_{2\omega}/P_{\omega}^{2} = 13\%\ W^{-1}$) CMOS-compatible SHG device to date. Most recently, this effect was taken into account by Castellan et al. while investigating SHG in silicon due to a straining silicon nitride layer[34]; this research may therefore provide the most recent and accurate calculation of $\chi^{(2)}$ in silicon. A comparison and history of these values has been compiled in Tab. 3.1 and Fig. 1.4.

Reference	Year	$\chi^{(2)}$ (pm/V)	η_{SHG}	stress (GPa)	Notes
Timurdogan[33]	2017	41 (quasi)	0.13 W^{-1} (quasi)	na	Quasi $\chi^{(2)}$ achieved via p-i-n junctions in silicon ridge waveguides
Borghi[32]	2016	8	na	-0.48	High-speed measurements carried out to rule out effects from EFISH
Schriever[31]	2015	0.6 - 11.4 (quasi)	na	-0.3 – > 1.2	SiO_2 and SiN_x stressing layers compared, EFISH effect of SiN_x confirmed via SHG
Damas[35]	2014	336	na	1	DC voltage measurement with SiN stressing layer, plasma dispersion effects likely
Chmielak[36]	2013	190	na	1	DC voltage $\chi^{(2)}$ and SiN stressing layer, waveguide width shown to affect $\chi^{(2)}$ value
Chmielak[3]	2011	122	na	na	DC voltage $\chi^{(2)}$, strain in Si measured via mapping Raman signal
Cazzanelli[37]	2011	40	10^{-8}	1.2	All optical experiment showing bulk $\chi^{(2)}$ via SHG, SiN stressing layer used
Bianco[38]	2011	20	10^{-8}	1.2	First SHG via a bulk $\chi^{(2)}$,all-optical, SiN stressing layer used
Jacobsen[27]	2006	15	na	1	First recorded bulk $\chi^{(2)}$, structure avoids EFISH effects

TABLE 3.1: Comparison of the most significant results regarding SHG in silicon (rows shaded red indicate results most likely include a plasma-dispersion effect, yellow indicates the effect of plasma dispersion is unknown)

Methodology and Results

4.1 Waveguide Types

Waveguides of different types and dimensions have been previously expertly fabricated by my colleague Charalambos Klitis. Fabrication was carried out using e-beam lithography followed by dry-etch processes. The fabricated geometries include strip-waveguides, slot-waveguides, and sub-wavelength grating (SWG) waveguides. The same sets of waveguides have also been fabricated with different claddings, which include: air, silicon dioxide, low-stress silicon nitride, and high-stress silicon nitride. An example of strip waveguide was depicted in Fig. 1.5a, and illustrations of slot and SWG waveguides shown in Figs. 4.1a and 4.1b respectively.

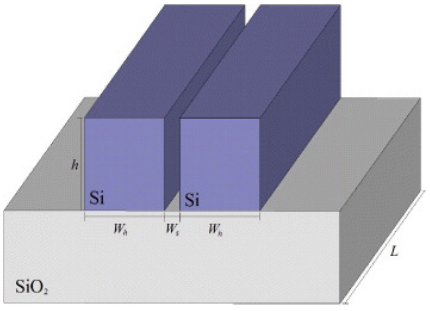

(A) Diagram of SOI slot waveguide[39]

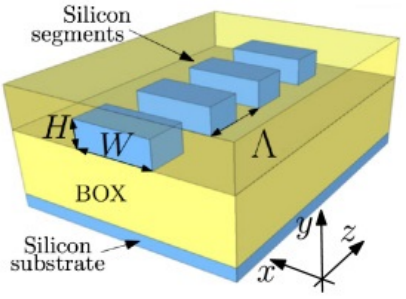

(B) Diagram of SOI SWG waveguide[40]

FIGURE 4.1

These different structures are each believed to have particular advantages which will be touched upon in Sec. 4.2.2. However, detailed analysis of slot and SWG waveguides is too large a body of work for this report and will be covered in future research. This report will mainly focus on results (from theory and measurement) of the strip waveguides.

4.2 Lumerical Simulations

4.2.1 Dispersion Engineering

The fabricated waveguides were designed for SHG, which is achieved via dispersion engineering. To confirm this, I imported the dimensions of the waveguides (from design) into Lumerical's mode solutions. This was to double check that the dimensions of the fabricated waveguides were correct for SHG using a pump wavelength at 3 μm. One way of changing the waveguide dispersion is to alter the width of the waveguide. Therefore, simulations of the effective index versus waveguide width were carried out for the fundamental mode at 3 μm and for multiple modes at 1.5 μm, which can be seen in Fig. 4.2.

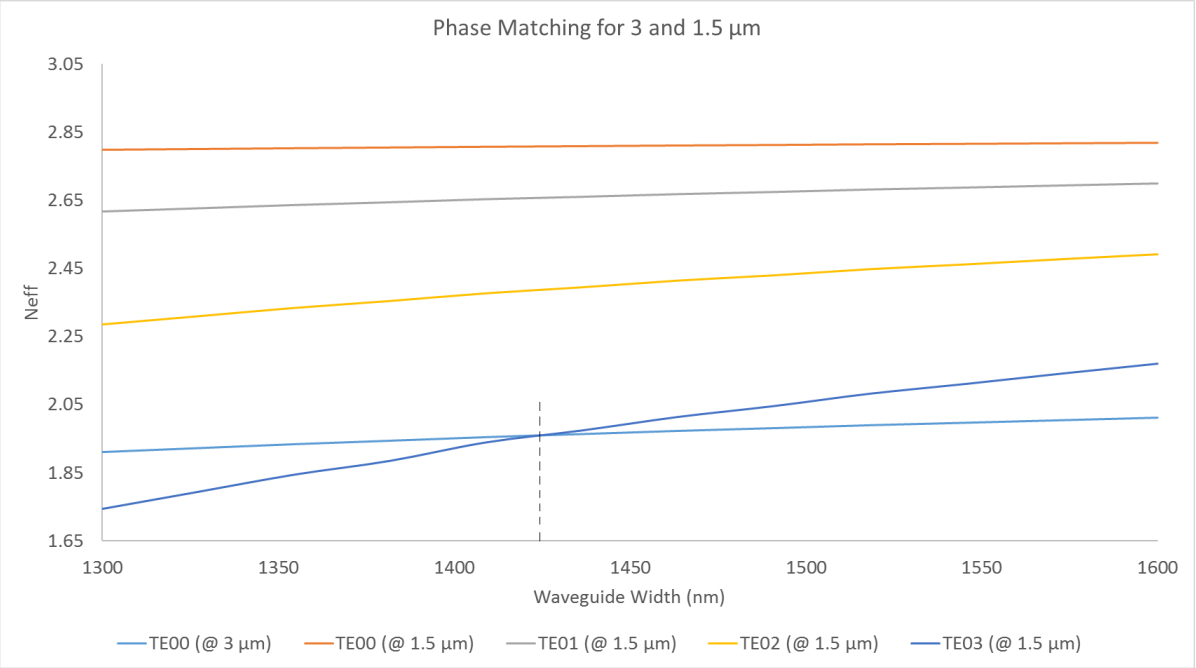

FIGURE 4.2: Waveguide dispersion: the effective refractive index is plotted against waveguide width for the fundamental mode at 3 μm and for multiple modes at 1.5 μm, with phase-matching occurring at width = 1427 nm (dashed line)

Therefore, from Fig. 4.2, it can be seen that the fundamental TE00 mode at 3 μm is phase-matched to the TE03 mode at 1.5 μm for a waveguide width of 1427 nm. Since the widths of the fabricated strip waveguides range from 1375-1950 nm, coupled with a degree of tunability of the laser source, means SHG should be achievable (for a reasonable phase-matching bandwidth).

4.2.2 Electric-field Comparison

As mentioned previously, surface $\chi^{(2)}$ in silicon is a result of the crystal lattice symmetry breaking at the surface. Considering this, the electric field profiles for a slot and strip waveguide propagating their fundamental modes at $\lambda = 3$ μm have been calculated using Lumerical's Mode Solutions, shown in Figs. 4.3 and 4.4. This was in order to compare the maximum electric field strength achieved at (or just below) the silicon surface.

Using this data, The E_y component of the electric field was plotted onto a cross-section of the structure for each waveguide, shown in Figs. 4.5 and 4.6. The strength of the electric field component E_y, and the maximum height of the waveguide have both been normalised to unity in these results.

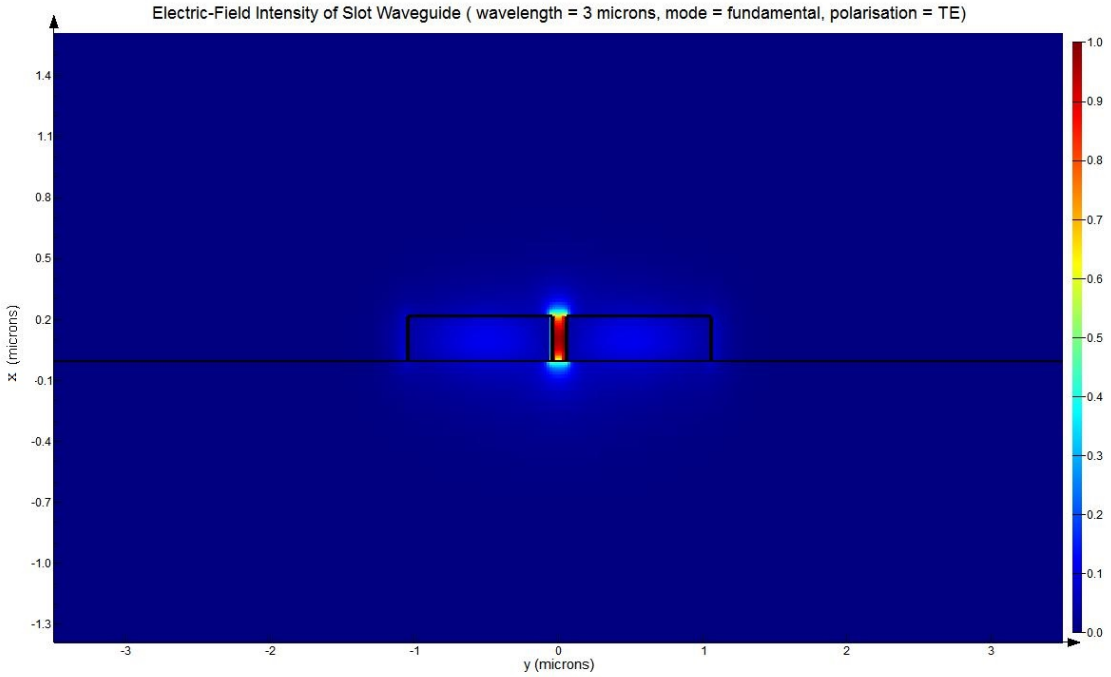

FIGURE 4.3: Electric field profile for a cross-section of a slot waveguide for the fundamental mode at 3 μm with TE polarisation. The electric field can be seen to be concentrated across the gap of the waveguide

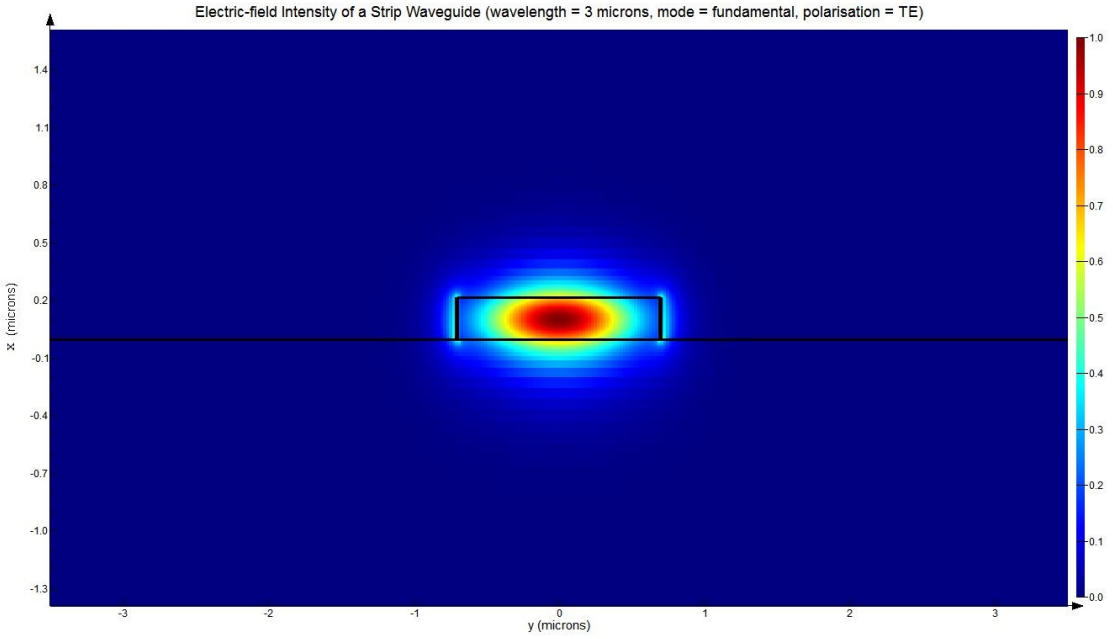

FIGURE 4.4: Electric field profile for a cross-section of a strip waveguide for the fundamental mode at 3 μm with TE polarisation. The electric field can be seen to be concentrated in the core of the waveguide

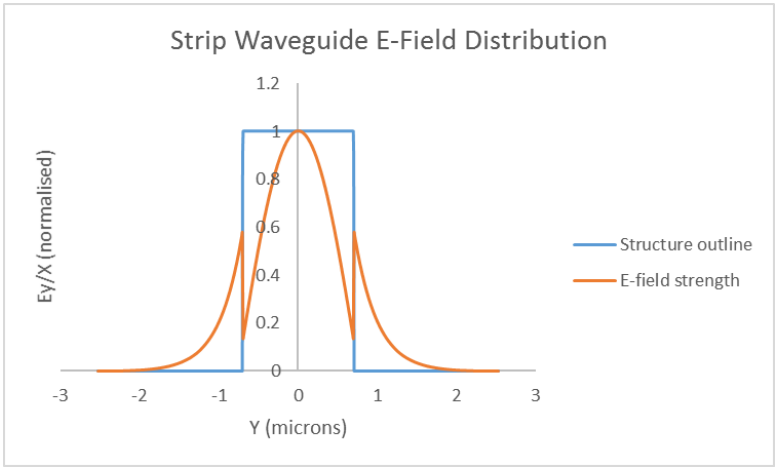

FIGURE 4.5: Plot of normalised electric field strength and waveguide cross-section of strip waveguide for the fundamental mode at 3 μm with TE polarisation

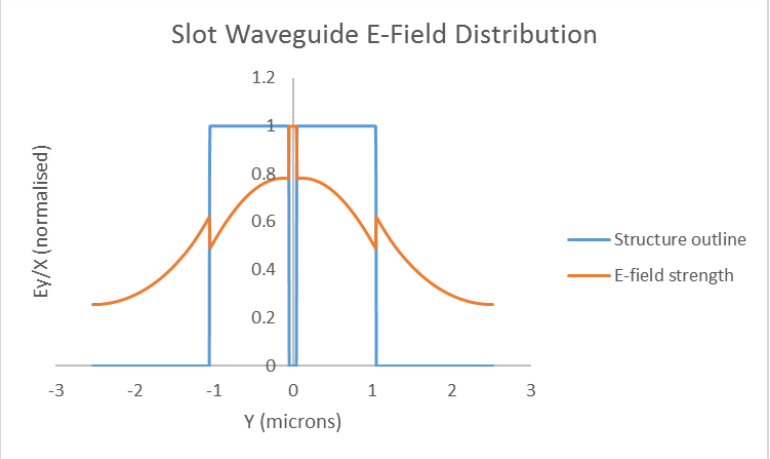

FIGURE 4.6: Plot of normalised electric field strength and waveguide cross-section of slot waveguide for the fundamental mode at 3 μm with TE polarisation

Upon analysis of these results, it can be seen that the maximum electric field strength on the silicon side of the waveguide interface is much higher for the slot waveguides (for the sides comprising the gap) compared to the strip waveguides. In theory, the slot waveguide should therefore enhance the surface $\chi^{(2)}$ more than the strip waveguide due to the higher electric field strength near the surface of the silicon (where crystal symmetry breaks). Therefore, part of this project will be looking into ways of exploiting this characteristic of slot waveguides to try and achieve enhanced $\chi^{(2)}$ values in silicon.

4.3 MATLAB Calculations

4.3.1 SHG Efficiency and Phase-matching Bandwidth

After confirming the dimensions of the waveguides are correct for phase-matching, the next stage was to model the type of SHG response to be expected from such waveguides. In order to plot the SHG efficiency, the phase mismatch must be calculated. By extracting the Lumerical data, polynomic functions could be fitted to the data, shown in Figs. 4.7 and 4.8. The resulting Δk, calculated using Eqn. 2.3.5, can be seen in Fig. 4.9.

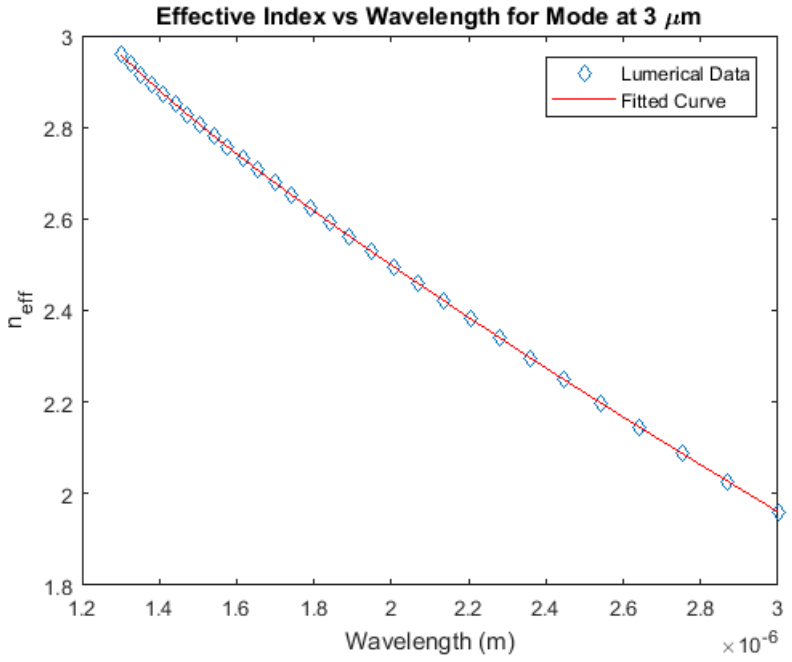

FIGURE 4.7

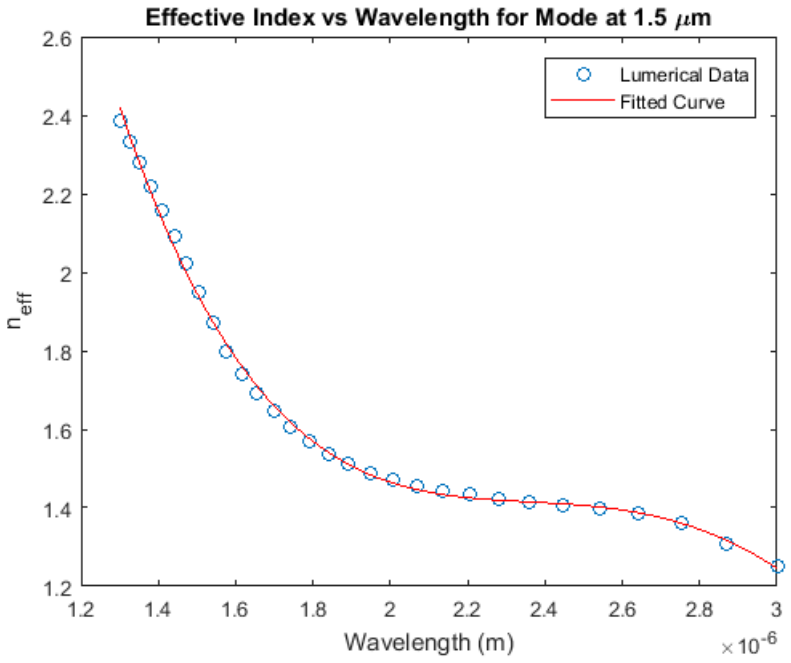

FIGURE 4.8

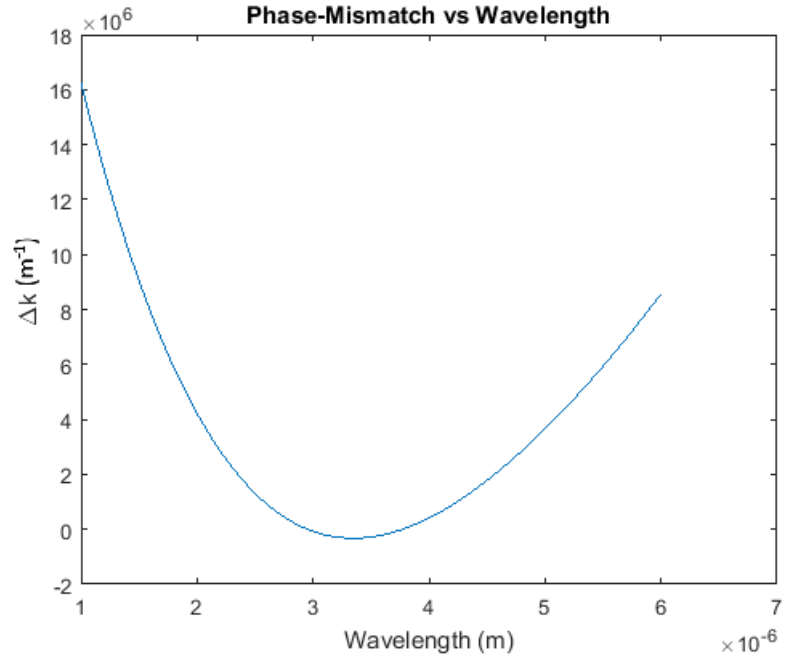

FIGURE 4.9

The SHG efficiency was calculated using Eqn. 2.3.1 and is shown in Fig. 4.10. The values for the maximum SHG efficiency and phase-matching bandwidth are given in Tab. 4.1, along with other relevant data.

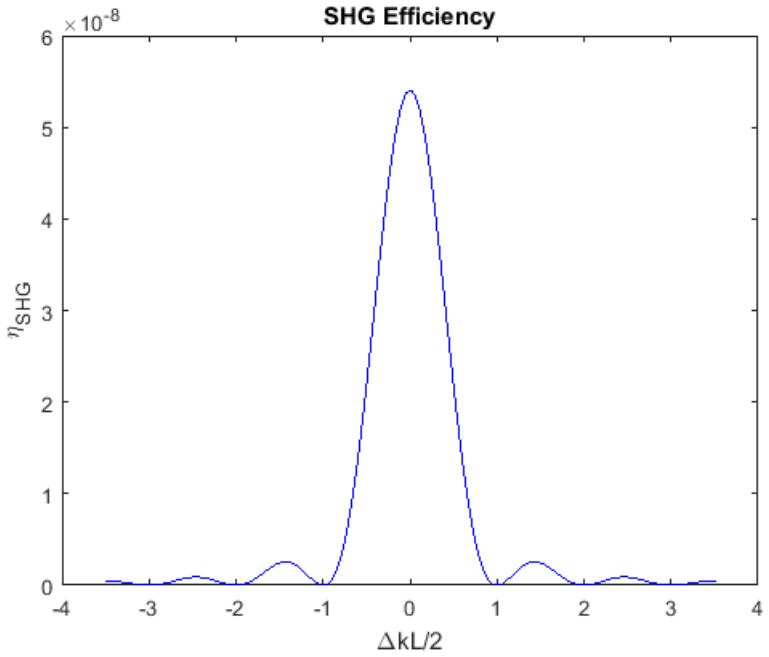

FIGURE 4.10

One variable that could be altered for future waveguides is the length. Therefore the effect of altering the length has been plotted for the phase-matching bandwidth and the maximum SHG efficiency in Figs. 4.11 and 4.12 respectively. From these graphs, a trade-off between the maximum SHG efficiency and phase-matching bandwidth can be seen.

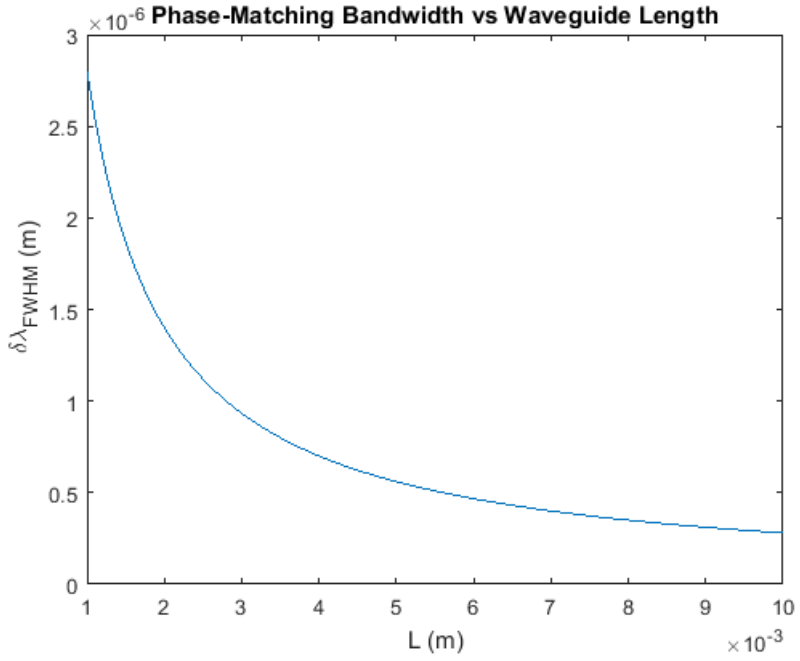

FIGURE 4.11

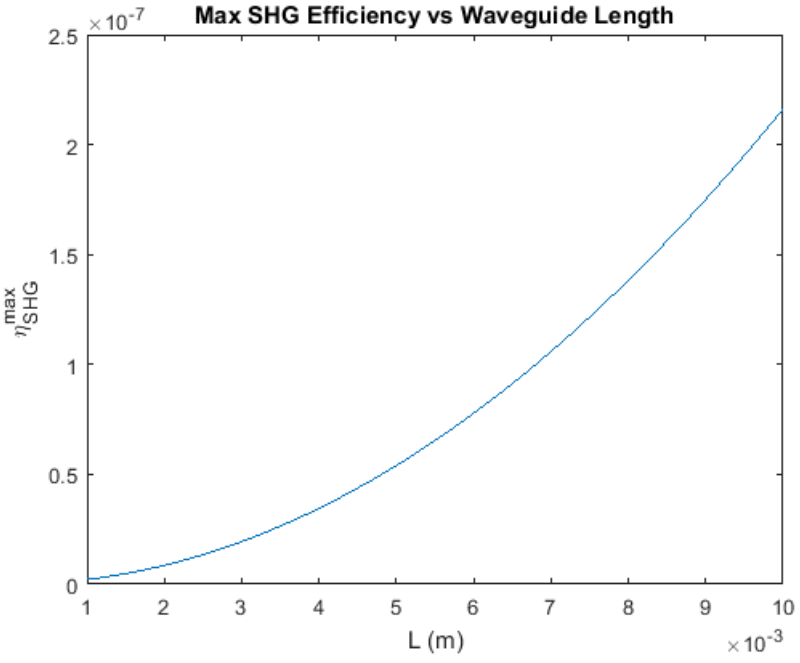

FIGURE 4.12

Property	Value	Notes
Max Power	1 W	Details of laser source
Peak Power	10 kW	
Pulse Duration	1-3 ps	
Wavelength Range	1-4 μm	
Repetition Rate	110 MHz	
$\chi^{(2)}$	5 pm/V	Conservative 2nd-order susceptibility value
Waveguide Length	5 mm	-
Numerical Aperture	0.65	Of lens focussing directly on to the waveguide
Average Input Power	25 mW	Measured directly from laser source ($\lambda = 3\ \mu m$) using power meter
Spotsize (diameter)	1.01 μm	Calculated using $spotsize = \frac{0.22\lambda}{NA}$
Peak Power	113.6 W (using 2 ps for Pulse Duration)	Calculated using $P_{peak} = \frac{P_{avg}}{RepetitionRate \times PulseDuration}$
Fundamental Intensity	141.8 GW/m^2 (using $r = 505nm$)	Calculated using $I_\omega = \frac{P_{peak}}{\pi r^2}$
Fundamental Intensity including losses	1.4 GW/m^2	Used for calculations, decrease due to Fresnel reflections of glass and silicon
Max. SHG Efficiency	5×10^{-8}	This result is comparable to that reported in the literature[37,38]
Phase-matching bandwidth	560 nm	Defined by the full width half max of $sinc(\Delta kL/2)^2$

TABLE 4.1: Table of technical and calculated values for obtaining results for the SHG efficiency and phase-matching bandwidth (rows highlighted in blue mean the results were calculated numerically using MATLAB)

4.3.2 Considerations

The main considerations of the results calculated in MATLAB are as follows:

- SHG efficiency calculated is comparable to that reported in the literature[37,38]
- The phase-matching bandwidth is suitably large enough to allow SHG (i.e. it should accommodate for deviations from the design due to fabrication tolerances)
- The effect of pulse compression/broadening due to ultrashort laser pulses has not been quantified, however, it is assumed that this will be negligible for pico-second pulses in this experiment
- Waveguide propagation loss has not been considered in these calculations yet, which will negatively impact results. A more accurate value for waveguide propagation loss (as opposed to the values from the multimode waveguides), would be to fabricate a single mode waveguide on the same sample to carry out standard loss measurements on (i.e. via the cut-back method) and use this value as a reference for how lossy the waveguides are
- The mode area of SHG signal needs to be calculated to then calculate the minimum power of the SHG signal and compare this to the minimum detection power of the detector ($\approx 1\ pW$)

4.4 Experimental Results

4.4.1 Waveguide Losses

Unfortunately, no SHG signals were detected during any of the measurements carried out over the course of this project. The lack of results can be attributed to multiple factors: limited time to learn new equipment and techniques, problems with equipment - specifically with the OPO laser which was not operational on multiple occasions while waiting for an engineer, and limited maximum power available from the OPO laser at 3 μm - meaning any SHG signals that may be generated have very low power.

The waveguides have, however, have been measured for losses using the Fabry-Pérot resonance model[41,18]. This was only carried out on the strip waveguides as the reflections from the slot and SWG waveguides would produce inaccurate values (due to the multiple boundaries). The attenuation constant was calculated using Eqn. 4.4.1, which only requires the reflectivity (R) and the ratio of the maximum and minimum intensities ($\zeta = \frac{I_{max}}{I_{min}}$) to be known. The value ζ was calculated using the constructive regions of the Fabry-Pérot data, an example of which is shown in Fig. 4.13.

$$\alpha = -\frac{1}{L} ln(\frac{1}{R}\frac{\sqrt{\zeta}-1}{\sqrt{\zeta}+1}) \tag{4.4.1}$$

Since the strip waveguides are designed to be multimode (to achieve SHG), the standalone value for the attenuation constant (α) may not be wholly accurate due to destructive interference that occurs between different modes[41]. However, it is worth mentioning that this destructive interference may only act to increase the value of the attenuation constant of the waveguide. Nonetheless, a comparison between these measurements can be useful for investigating the relative losses of the waveguides due to the different claddings present, shown in Tab. 4.2.

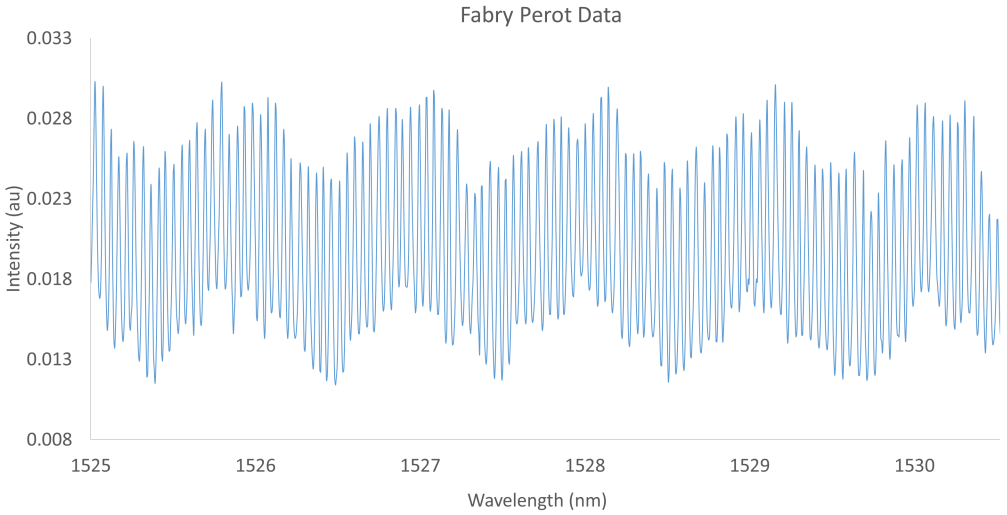

FIGURE 4.13: Fabry-Pérot reflections for multimode strip waveguide used to calculate attenuation constant, the lower frequency sinusoidal response that can be seen is due to interference of different modes within the waveguide

Waveguide Width (nm)	**Cladding Type**	**Avg. Loss ($dBcm^{-1}$)**
1375	air	0.6
1375	SiO_2	0.7
1375	SiN Low Stress	1.6
1375	SiN High Stress	1.6

TABLE 4.2: Comparison of Fabry-Pérot resonance calculated attenuation constant values for different waveguide widths and cladding types

4.4.2 Experimental SHG Set-Up

A photo and illustration of the experimental set-up that will be used for the measuring SHG from the silicon waveguides is shown in Figs. 4.14 and 4.15 respectively. In this set-up, the band-pass filter is centred at 3 μm, this is in order to filter out any pump signal (at 1040 nm) that may come from the OPO laser.A short-pass filter was also used to ensure the detector only receives a SHG signal (with wavelengths above 1.5 μm being filtered out).

A reflective objective lens was used for focussing light into the waveguide; this was advantageous over a refractive objective lens as it meant the input laser could be switched from 1550 nm to 3 μm (OPO laser) without having to adjust for the focal length of the input objective. The 1550 nm laser was used to ensure the setup was in alignment and was optimised for detecting the expected SHG emission at 1.5 μm . The IR camera and monitor were used to establish that successful propagation had been achieved when using the 1550 nm laser. This signal was then optimisation using a combination of the chopper, lock-in amplifier, detector and oscilloscope; the positioning and focus of the output lens was adjusted to maximise the signal received by the oscilloscope. When measuring waveguide losses (discussed in Section 4.4.1), the detector was replaced with a FTIR.

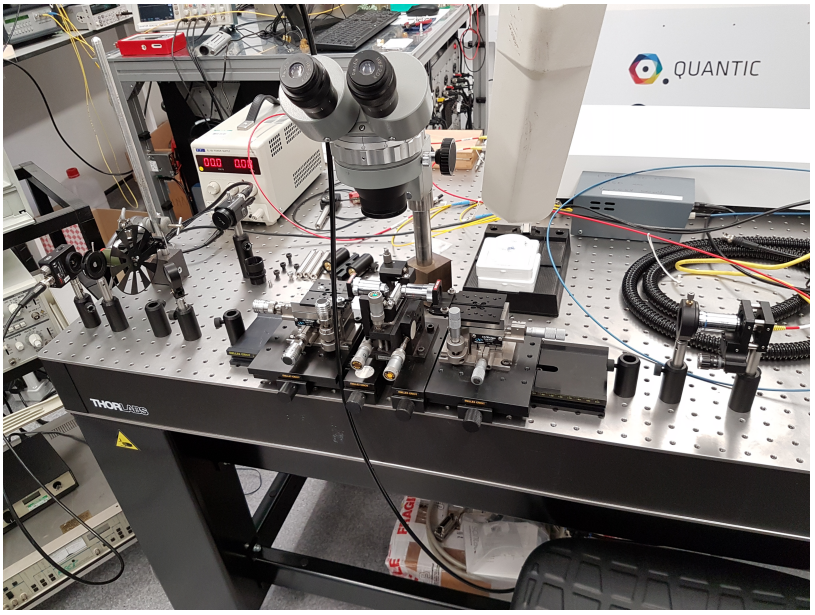

FIGURE 4.14: Photo of experimental set-up for achieving SHG (empty optical posts are for filters)

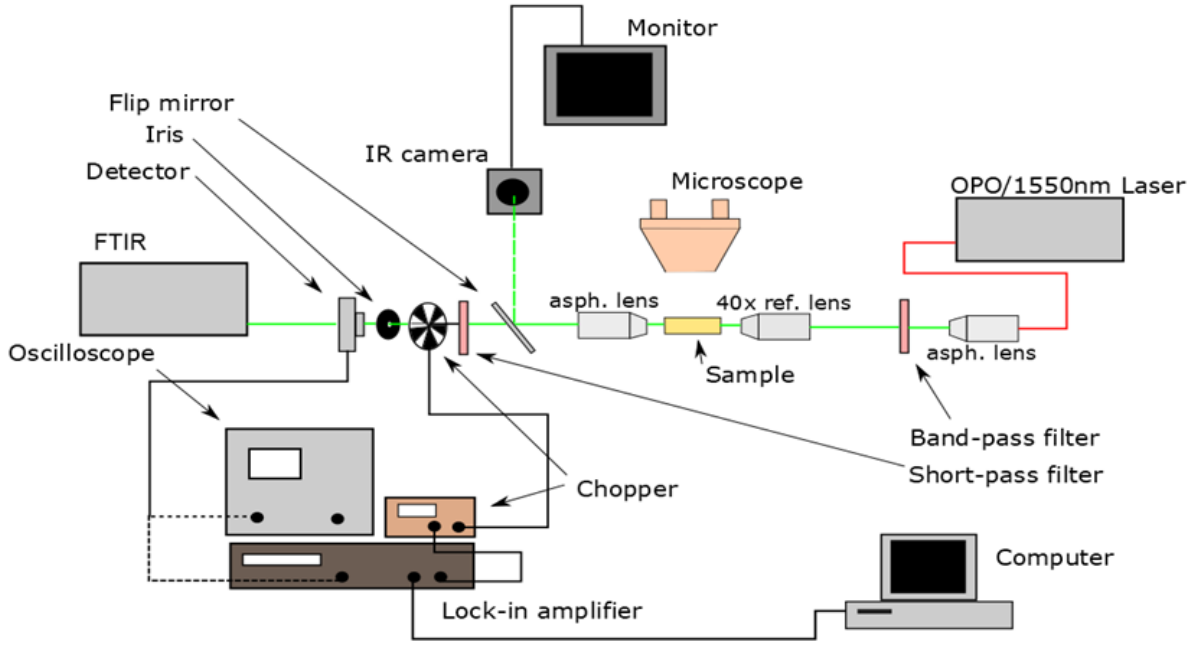

FIGURE 4.15: Diagram detailing the experimental set-up for achieving SHG

4.4.3 FTIR Measurements

The OPO laser was tuned to 3 μm using a Thorlabs FTIR. The best spectrum that could be achieved, targeting 3 μm, can be seen in Fig. 4.16. The total power measured from the OPO, while giving this output, was measured to be approximately 30 mW.

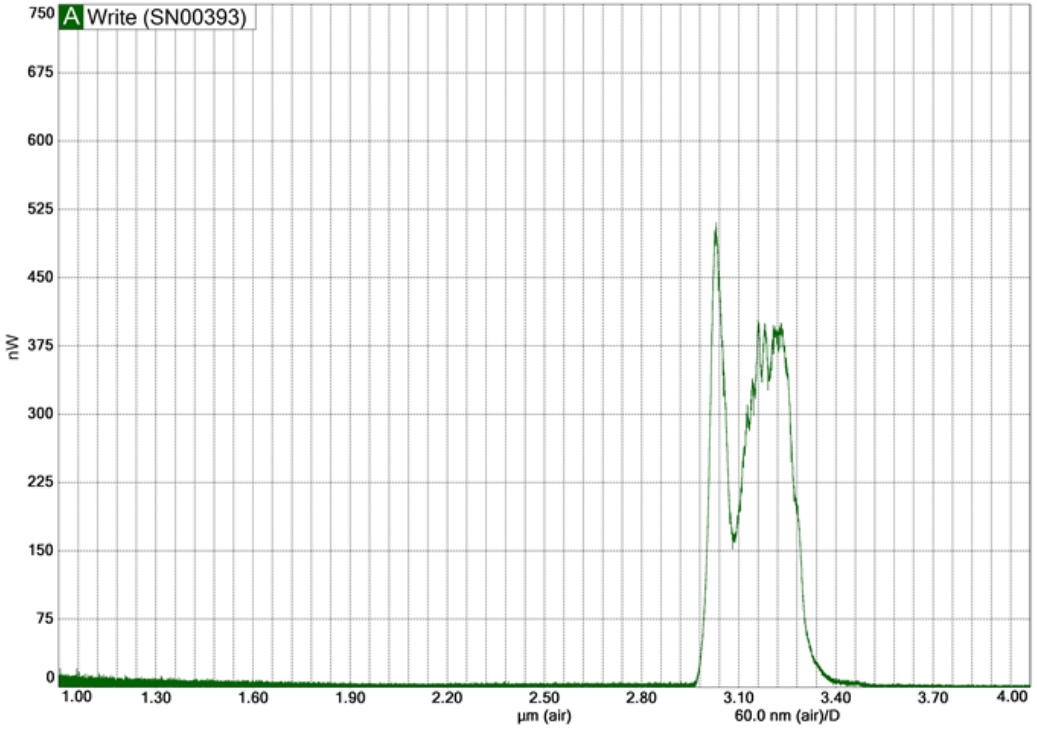

FIGURE 4.16: Direct spectrum of OPO laser output measured using a FTIR

The transmission of the bandpass filter is shown in Fig. 4.17. The power measured directly after the bandpass filter was measured to be approximately 25 mW.

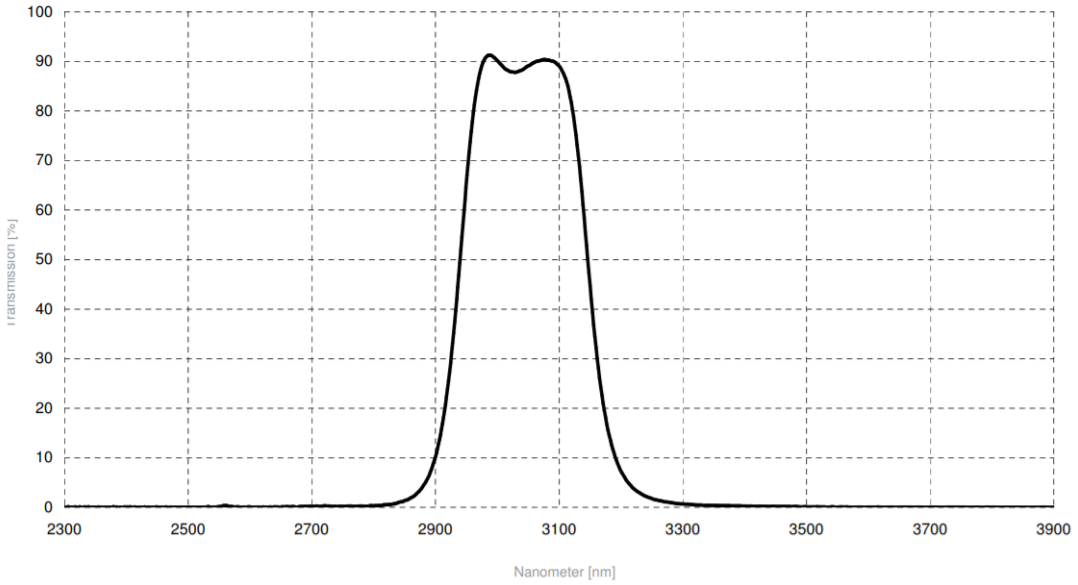

FIGURE 4.17: Transmission spectrum of the bandpass filter used in the experimental set-up

After aligning the set-up with the 1550 nm laser - observing light being guided through the waveguides - the input was switched from the 1550 nm laser to the OPO laser. To ensure the light was still being guided through the waveguides, the FTIR was used to measure the signal for light passing through one of the slab waveguides. The result of this can be seen in Fig. 4.18, where the OPO signal can clearly be seen to have been guided through the waveguide.

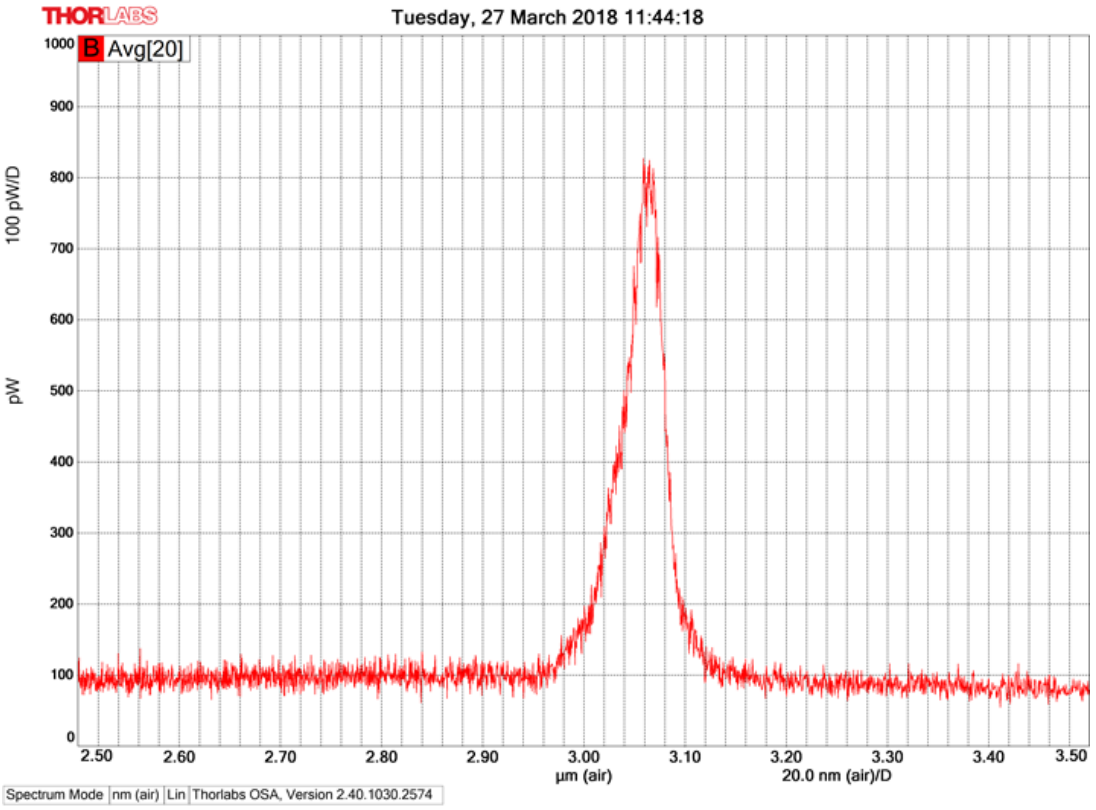

FIGURE 4.18: Spectrum of output measured from waveguide, with OPO laser as the input, using the FTIR

Future Research

Future research which may expand upon these results can be broken down into the following areas:

- Increase the available power at 3 μm or change the design of the waveguides so that phase-matching occurs at a different wavelength where more power/sensitivity may be available
- Utilise a high speed detector to take advantage of the high peak powers of the OPO laser, or alternatively, use a camera with a very high sensitivity and a long integration time to detect low power SHG signals
- Model SHG signal from slot and SWG waveguides and compare to experimental results
- Once a SHG signal has been detected , investigate the effect of different claddings on the SHG signal/$\chi^{(2)}$ value
- Measure SHG signal of slot and SWG waveguides and compare effectiveness of different geometries for SHG efficiency
- Use most successful geometry (highest SHG efficiency) and cladding for carrying out spontaneous parametric down-conversion (SPDC) for quantum experiments/applications

Appendix

A.1 Lumerical Scriping

In this section, the code written in order to calculate the phase-matching conditions for the silicon waveguides using Lumerical software is given.

Lumerical Code for Calculating Phasematching

```
switchtolayout;
clear;
cleardcard;


WGwidth = linspace(2.0e-6,0.5e-6,51);    # Desired waveguide width range goes here

neff1 = matrix(length(WGwidth));    # Initialising effective index values
neff2 = matrix(length(WGwidth));    # for the different modes
neff3 = matrix(length(WGwidth));
neff4 = matrix(length(WGwidth));
neff5 = matrix(length(WGwidth));
neff6 = matrix(length(WGwidth));

neff1b = matrix(length(WGwidth)); # Initialising effective index for 3 um mode



for(i=1:length(WGwidth)) {
  switchtolayout;
  setnamed("mesh","x span", WGwidth(i));       # Make sure names and object
  setnamed("waveguide","x span", WGwidth(i)); # orientations match here - i.e.
  run; mesh;                                   # waveguide width is in the x-direction
  setanalysis('wavelength',1.5e-6);    # Enter desired wavelength here
  findmodes;

  if (i==1){
    copydcard('mode1','m1'); #neff1    # Stores initial effective index values of each
    copydcard('mode2','m2'); #neff2    # modes here i.e. for widest width
    copydcard('mode3','m3'); #neff3    # of waveguide, that is  i = 1
    copydcard('mode4','m4'); #neff4
    copydcard('mode5','m5'); #neff5
    copydcard('mode6','m6'); #neff5
  }

  neff1(i) = real(getdata(bestoverlap('m1'),'neff'));    # Effective index values of each
  neff2(i) = real(getdata(bestoverlap('m2'),'neff'));    # mode are tracked (using
  neff3(i) = real(getdata(bestoverlap('m3'),'neff'));    # bestoverlap) and stored here
  neff4(i) = real(getdata(bestoverlap('m4'),'neff'));
  neff5(i) = real(getdata(bestoverlap('m5'),'neff'));
  neff6(i) = real(getdata(bestoverlap('m6'),'neff'));
```

```
  if (neff3(i) == neff1(i)){neff3(i) = 0;}     # This section is to prevent modes
  if (neff4(i) == neff2(i)){neff4(i) = 0;}     # reappearing once the have gone past cut-off
  if (neff5(i) == neff1(i)){neff5(i) = 0;}
  if (neff5(i) == neff3(i)){neff5(i) = 0;}
  if (WGwidth(i) < 1.4e-6){neff5(i) = 0;}



}


#for second wavelength, same method as above

switchtolayout;
cleardcard;

for(i=1:length(WGwidth)) {
  switchtolayout;
  setnamed("mesh","x span", WGwidth(i));
  setnamed("waveguide","x span", WGwidth(i));
  run; mesh;
  setanalysis('wavelength',2.5e-6);
  findmodes;

  if (i==1){
    copydcard('mode1','m1');
  }

  neff1b(i) = real(getdata(bestoverlap('m1'),'neff'));#-slab_neff;

}



# Plot results
plot(WGwidth*1e6,neff1b,neff1,neff2,neff3,neff4,neff5,neff6,'waveguide width (um)','neff');
legend("mode1 (3um)","mode1","mode2","mode3","mode4","mode5","mode6");
```

Bibliography

[1] Laurent Vivien. *Handbook of silicon photonics*. Taylor & Francis, Boca Raton, FL, 2013.

[2] Richard Sutherland. *Handbook of nonlinear optics*. Marcel Dekker, New York, 2003.

[3] Bartos Chmielak, Michael Waldow, Christopher Matheisen, Christian Ripperda, Jens Bolten, Thorsten Wahlbrink, Michael Nagel, Florian Merget, and Heinrich Kurz. Pockels effect based fully integrated, strained silicon electro-optic modulator. *OPTICS EXPRESS*, 19(18):17212–17219, AUG 29 2011.

[4] Luca Alloatti, Robert Palmer, Sebastian Diebold, Kai Philipp Pahl, Baoquan Chen, Raluca Dinu, Maryse Fournier, Jean-Marc Fedeli, Thomas Zwick, Wolfgang Freude, and et al. 100 ghz silicon-organic hybrid modulator. *Light: Science & Applications*, 3(5), 2014.

[5] The Chip that Jack Built. http://www.ti.com/corp/docs/kilbyctr/jackbuilt.shtml. *Texas Instruments*, Accessed: 04-05-2017.

[6] GE Moore. Cramming more components onto integrated circuits (Reprinted from Electronics, pg 114-117, April 19, 1965). *PROCEEDINGS OF THE IEEE*, 86(1):82–85, JAN 1998.

[7] Altera's 30 billion transistor FPGA. http://www.gazettabyte.com/home/2015/6/28/alte 30-billion-transistor-fpga.html. *Gazettabyte*, Accessed: 04-05-2017.

[8] Silicon Photonics Course. http://www.helios-project.eu/download/silicon-photonics-course. *HELIOS*, Accessed: 04-05-2017.

[9] Copper Interconnects: The Evolution of Microprocessors. http://www-03.ibm.com/ibm/history/ibm100/us/en/icons/copperchip/. *IBM*, Accessed: 04-05-2017.

[10] Lorenzo Pavesi. *Optical interconnects : the silicon approach*. Springer, Berlin New York, 2006.

[11] P Gargini, J Glaze, and O Williams. The SIA's 1997 National Technology Roadmap for Semiconductors. *SOLID STATE TECHNOLOGY*, 41(1):73+, JAN 1998.

[12] Resources. https://www.semiconductors.org/main/resources/. *Semiconductor Industry Association*, Accessed: 05-05-2017.

[13] Nir Magen, Avinoam Kolodny, Uri Weiser, and Nachum Shamir. Interconnect-power dissipation in a microprocessor. *Proceedings of the 2004 international workshop on System level interconnect prediction - SLIP '04*, 2004.

[14] Minimize IC power without sacrificing performance. http://www.eetimes.com/document.asp?doc_id=1217833. *EE Times*, Accessed: 05-05-2017.

[15] Lukas Chrostowski. *Silicon photonics design*. Cambridge University Press, Cambridge New York, 2015.

[16] Bahrain Jalali and Sasan Fathpour. Silicon photonics. *JOURNAL OF LIGHTWAVE TECHNOLOGY*, 24(12):4600–4615, DEC 2006.

[17] RA SOREF and JP LORENZO. ALL-SILICON ACTIVE AND PASSIVE GUIDED-WAVE COMPONENTS FOR LAMBDA=1.3 AND 1.6 MU-M. *IEEE JOURNAL OF QUANTUM ELECTRONICS*, 22(6):873–879, JUN 1986.

[18] G. T. Reed, G. Mashanovich, F. Y. Gardes, and D. J. Thomson. Silicon optical modulators. *NATURE PHOTONICS*, 4(8):518–526, AUG 2010.

[19] J. Leuthold, C. Koos, and W. Freude. Nonlinear silicon photonics. *NATURE PHOTONICS*, 4(8):535–544, AUG 2010.

[20] Robert W. Boyd. *Nonlinear Optics, Third Edition*. Academic Press, Inc., USA, 2008.

[21] R. Dekker, N. Usechak, M. Forst, and A. Driessen. Ultrafast nonlinear all-optical processes in silicon-on-insulator waveguides. *JOURNAL OF PHYSICS D-APPLIED PHYSICS*, 40(14):R249–R271, JUL 21 2007.

[22] Massimo Cazzanelli and Joerg Schilling. Second order optical nonlinearity in silicon by symmetry breaking. *APPLIED PHYSICS REVIEWS*, 3(1), MAR 2016.

[23] HWK TOM, TF HEINZ, and YR SHEN. 2ND-HARMONIC REFLECTION FROM SILICON SURFACES AND ITS RELATION TO STRUCTURAL SYMMETRY. *PHYSICAL REVIEW LETTERS*, 51(21):1983–1986, 1983.

[24] SV GOVORKOV, VI EMELYANOV, NI KOROTEEV, GI PETROV, IL SHUMAY, and VV YAKOVLEV. INHOMOGENEOUS DEFORMATION OF SILICON SURFACE-LAYERS PROBED BY 2ND-HARMONIC GENERATION IN REFLECTION. *JOURNAL OF THE OPTICAL SOCIETY OF AMERICA B-OPTICAL PHYSICS*, 6(6):1117–1124, JUN 1989.

[25] JY HUANG. PROBING INHOMOGENEOUS LATTICE DEFORMATION AT INTERFACE OF SI(111)/SIO2 BY OPTICAL 2ND-HARMONIC REFLECTION AND RAMAN-SPECTROSCOPY. *JAPANESE JOURNAL OF APPLIED PHYSICS PART 1-REGULAR PAPERS SHORT NOTES & REVIEW PAPERS*, 33(7A):3878–3886, JUL 1994.

[26] JI Dadap, Z Xu, XF Hu, MC Downer, NM Russell, JG Ekerdt, and OA Aktsipetrov. Second-harmonic spectroscopy of a Si(001) surface during calibrated variations in temperature and hydrogen coverage. *PHYSICAL REVIEW B*, 56(20):13367–13379, NOV 15 1997.

[27] RS Jacobsen, KN Andersen, PI Borel, J Fage-Pedersen, LH Frandsen, O Hansen, M Kristensen, AV Lavrinenko, G Moulin, H Ou, C Peucheret, B Zsigri, and A Bjarklev. Strained silicon as a new electro-optic material. *NATURE*, 441(7090):199–202, MAY 11 2006.

[28] Clemens Schriever, Christian Bohley, and Ralf B. Wehrspohn. Strain dependence of second-harmonic generation in silicon. *OPTICS LETTERS*, 35(3):273–275, FEB 1 2010.

[29] Matteo Galli, Dario Gerace, Karl Welna, Thomas F. Krauss, Liam O'Faolain, Giorgio Guizzetti, and Lucio Claudio Andreani. Low-power continuous-wave generation of visible harmonics in silicon photonic crystal nanocavities. *OPTICS EXPRESS*, 18(25):26613–26624, DEC 6 2010.

[30] S. Sharif Azadeh, F. Merget, M. P. Nezhad, and J. Witzens. On the measurement of the Pockels effect in strained silicon. *OPTICS LETTERS*, 40(8):1877–1880, APR 15 2015.

[31] Clemens Schriever, Federica Bianco, Massimo Cazzanelli, Mher Ghulinyan, Christian Eisenschmidt, Johannes de Boor, Alexander Schmid, Johannes Heitmann, Lorenzo Pavesi, and Jörg Schilling. Second-order optical nonlinearity in silicon waveguides: Inhomogeneous stress and interfaces. *Advanced Optical Materials*, 3(1):129–136, 2015.

[32] Massimo Borghi, Mattia Mancinelli, Florian Merget, Jeremy Witzens, Martino Bernard, Mher Ghulinyan, Georg Pucker, and Lorenzo Pavesi. High frequency electro optic measurement of strained silicon racetrack resonators. In Vivien, L and Pavesi, L and Pelli, S, editor, *SILICON PHOTONICS AND PHOTONIC INTEGRATED CIRCUITS V*, volume 9891 of *Proceedings of SPIE*, 1000 20TH ST, PO BOX 10, BELLINGHAM, WA 98227-0010 USA, 2016. SPIE; Brussels Photon Team; Res Fdn Flanders; Visit Brussels, SPIE-INT SOC OPTICAL ENGINEERING. Conference on Silicon Photonics and Photonic Integrated Circuits V, Brussels, BELGIUM, APR 03-07, 2016.

[33] E. Timurdogan, C. V. Poulton, M. J. Byrd, and M. R. Watts. Electric field-induced second-order nonlinear optical effects in silicon waveguides. *NATURE PHOTONICS*, 11(3):200+, MAR 2017.

[34] Claudio Castellan, Alessandro Trenti, Chiara Vecchi, Alessandro Marchesinia, Mattia Mancinelli, Mher Ghulinyan, George Pucker, and Lorenzo Pavesi. On the origin of second harmonic generation in silicon waveguides with silicon nitride cladding. *Scientific Reports*, 2019.

[35] Pedro Damas, Xavier Le Roux, David Le Bourdais, Eric Cassan, Delphine Marris-Morini, Nicolas Izard, Thomas Maroutian, Philippe Lecoeur, and Laurent Vivien. Wavelength dependence of Pockels effect in strained silicon waveguides. *OPTICS EXPRESS*, 22(18):22095–22100, SEP 8 2014.

[36] Bartos Chmielak, Christopher Matheisen, Christian Ripperda, Jens Bolten, Thorsten Wahlbrink, Michael Waldow, and Heinrich Kurz. Investigation of local strain distribution and linear electro-optic effect in strained silicon waveguides. *OPTICS EXPRESS*, 21(21):25324–25332, OCT 21 2013.

[37] M. Cazzanelli, F. Bianco, E. Borga, G. Pucker, M. Ghulinyan, E. Degoli, E. Luppi, V. Véniard, S. Ossicini, and D. et al. Modotto. Second-harmonic generation in silicon waveguides strained by silicon nitride. *Nature Materials*, 11(2):148–154, 2011.

[38] F. Bianco, E. Borga, A. Yeremian, B. Dierre, K. Fedus, P. Bettotti, A. Pitanti, R. Pierobon, M. Ghulinyan, G. Pucker, M. Cazzanelli, and L. Pavesi. Second-order susceptibility $\chi^{(2)}$ in Si waveguides. *IEEE International Conference on Group IV Photonics GFP*, (2):27–29, 2011.

[39] B. Radjenovic, B. Milanovic, and M. Radmilovic-Radjenovic. Electric field enhancement in silicon slotted optical strip waveguides and microring resonators. *PHYSICA SCRIPTA*, T149, APR 2012. 3rd International School and Conference on Photonics, Belgrade, SERBIA, AUG 29-SEP 02, 2011.

[40] J. Dario Sarmiento-Merenguel, Alejandro Ortega-Monux, Jean-Marc Fedeli, J. Gonzalo Wanguemert-Perez, Carlos Alonso-Ramos, Elena Duran-Valdeiglesias, Pavel Cheben, Inigo Molina-Fernandez, and Robert Halir. Controlling leakage losses in subwavelength grating silicon metamaterial waveguides. *OPTICS LETTERS*, 41(15):3443–3446, AUG 1 2016.

[41] A De Rossi, V Ortiz, M Calligaro, L Lanco, S Ducci, V Berger, and I Sagnes. Measuring propagation loss in a multimode semiconductor waveguide. *JOURNAL OF APPLIED PHYSICS*, 97(7), APR 1 2005.